Validation of OMI tropospheric NO_2 column densities using direct-Sun mode Brewer measurements at NASA Goddard Space Flight Center

M. O. Wenig,[1,2] A. M. Cede,[3] E. J. Bucsela,[1] E. A. Celarier,[4] K. F. Boersma,[5] J. P. Veefkind,[6] E. J. Brinksma,[6] J. F. Gleason,[7] and J. R. Herman[7]

Received 17 May 2007; revised 29 January 2008; accepted 9 April 2008; published 9 July 2008.

[1] This paper presents a comparison of NO_2 data measured with the Ozone Monitoring Instrument (OMI) on board the EOS-AURA satellite with ground-based direct-Sun Brewer measurement data. Since its deployment in July 2004, OMI has provided more than 2 years of daily high-resolution ($\sim 13 \times 24$ km^2 at nadir) NO_2 vertical column density maps. We describe the retrieval, which includes an estimation of the stratospheric and tropospheric fraction of total NO_2 columns, the air mass factor (AMF) correction based on detected tropospheric NO_2 enhancements, and the generation of the gridded data product. We present a validation study of the gridded NO_2 data set using data from a Brewer MK3 double monochromator in direct-Sun mode located at NASA Goddard Space Flight Center in Greenbelt, Maryland, USA. Monthly averages of coinciding measurements correlate well (r = 0.9) but OMI data are about 25% lower than the Brewer measurement data (slope 0.75, intercept -0.38×10^{15} molecules/cm^2). We present a detailed uncertainty analysis for both ground and satellite data and discuss the possible reasons for the observed differences.

Citation: Wenig, M. O., A. M. Cede, E. J. Bucsela, E. A. Celarier, K. F. Boersma, J. P. Veefkind, E. J. Brinksma, J. F. Gleason, and J. R. Herman (2008), Validation of OMI tropospheric NO_2 column densities using direct-Sun mode Brewer measurements at NASA Goddard Space Flight Center, *J. Geophys. Res.*, *113*, D16S45, doi:10.1029/2007JD008988.

1. Introduction

[2] On 15 July 2004, the EOS-AURA satellite was launched on a mission to study the composition, chemistry and dynamics of the Earth's atmosphere and to improve our understanding of air quality and climate. One of Aura's instruments is the Ozone Monitoring Instrument (OMI), an imaging spectrometer that measures trace gas amounts such as ozone and nitrogen dioxide (NO_2).

[3] While NO_2 is an atmospheric pollutant that is toxic at high concentrations, its particular importance lies in its influence on atmospheric ozone chemistry. NO_X (= NO + NO_2) takes part in catalytic destruction of ozone in the stratosphere [*Crutzen*, 1970], while in the boundary layer NO_x is a catalyst for tropospheric ozone formation. Acid rain, caused by the release of NO_X, is known to ecologically damage lakes and forests. NO_2 may also play a significant role in radiative heating of the atmosphere [*Solomon et al.*, 1999].

[4] The main sources of tropospheric NO_X are industry (e.g., power generation) and traffic, forest and bush fires [*Crutzen and Schmailzl*, 1983], microbiological emissions by soil [*Granli and Bokman*, 1994], exchange with the stratosphere, lightning [*Beirle et al.*, 2005] and air traffic. It is estimated that more than half of the total NOx emissions are anthropogenic, dominated by the burning of fossil fuels for transportation and industrial activities [*Lee et al.*, 1997].

[5] The history of ground-based studies of stratospheric NO_2 begins with measurements by *Brewer et al.* [1973], *Noxon* [1975, 1979], *Noxon et al.* [1979] and *Solomon and Garcia* [1984]. Since 1995 data from the Global Ozone Monitoring Instrument (GOME, launched in 1995) [*Burrows et al.*, 1999b] have been used to retrieve global NO_2 column amounts. More recently, improved satellite instruments have been deployed: e.g., the Scanning Imaging Absorption Spectrometer for Atmospheric Chartography (SCIAMACHY, launched in 2002) [*Bovensmann et al.*, 1999], and finally Ozone Measuring Instrument (OMI, launched in 2004) with better spatial and temporal resolution.

[6] To validate satellite-derived NO_2 column amounts over polluted areas, measurement techniques that do not primarily rely on estimations of the air mass factor (AMF) are of great advantage. This can be obtained, e.g., by airborne in situ profile measurements [*Heland et al.*, 2002; *Martin et al.*, 2004], or by direct-Sun observations [*Brewer*

[1]NASA GSFC, Goddard Earth Sciences and Technology Center, University of Maryland, Baltimore County, Baltimore, Maryland, USA.
[2]Now at Department of Physics and Materials Science, City University of Hong Kong, Kowloon, Hong Kong.
[3]NASA GSFC, Earth System Science Interdisciplinary Center, University of Maryland, College Park, Maryland, USA.
[4]NASA GSFC, SGT Inc., Greenbelt, Maryland, USA.
[5]Department of Atmospheric Chemistry, Harvard University, Cambridge, Massachusetts, USA.
[6]Royal Netherlands Meteorological Institute, De Bilt, Netherlands.
[7]NASA Goddard Space Flight Center, Greenbelt, Maryland, USA.

Copyright 2008 by the American Geophysical Union.
0148-0227/08/2007JD008988

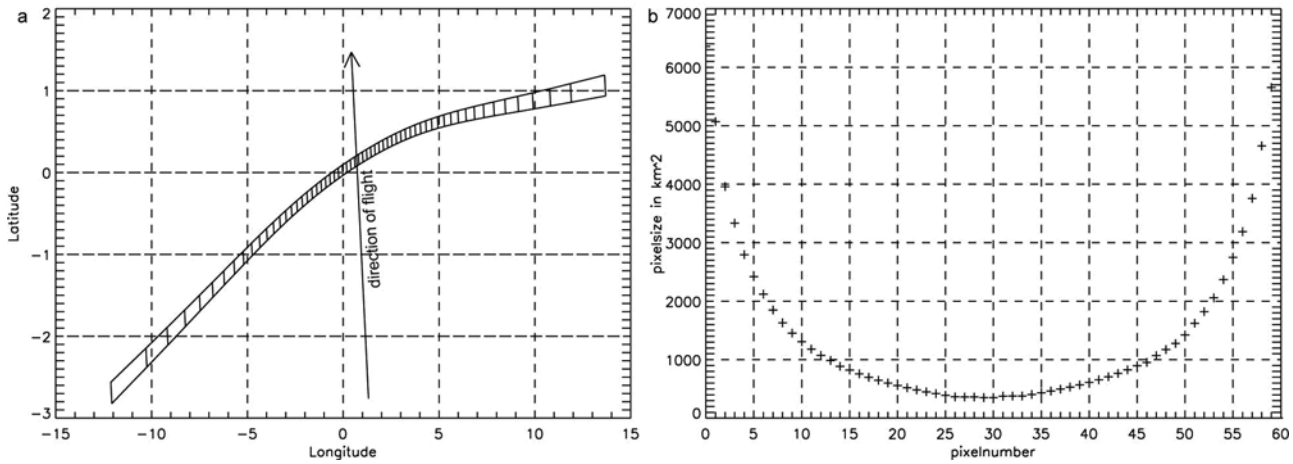

Figure 1. (a) The position of the 60 ground pixels for an OMI measurement in the tropics. Note that the x and *y* axis cover a different distance on the Earth's surface. (b) The size of the OMI pixels as a function of the across track pixel number.

et al., 1973; *Cede et al.*, 2006], where the influence of atmospheric parameters on the AMF is negligible. While airborne measurements are usually limited to a few days during a validation campaign, ground-based data can be collected continuously over an extended period. In this paper we validate the first 29 months of OMI's NO_2 column content with ground-based measurements obtained using a Brewer spectrometer at Goddard Space Flight Center (GSFC), near Washington DC, USA.

2. OMI Instrument

[7] The Aura satellite is in a near-polar, Sun-synchronous orbit with a 1345 local time equator crossing time. OMI has provided more than 2 years of daily global high-resolution NO_2 vertical column density data. The instrument consists of two nadir-viewing imaging spectrometers measuring the UV/VIS spectral range from 270 nm to 500 nm with a spectral resolution between 0.45 nm and 1.0 nm FWHM. The spectral sampling is two to three times the spectral resolution.

[8] OMI uses two CCDs with 780 × 576 pixels each. The first dimension spans the spectral wavelengths, and the second dimension is rebinned to provide measurements at 60 positions across the orbital track every 2 s (see Figure 1a). In the global observation mode, the 60 measurements cover a swath of approximately 2600 km. Because of optical aberrations and asymmetric alignment between the instrument's optical axis and the spacecraft axes, the ground pixels are not symmetrically aligned with respect to the orbital plane. The pixel size is 13 × 24 km^2 at nadir, and increase in size off nadir (see Figure 1b) to ~40 × 160 km^2 at the two ends of the track. The change in pixel size, and hence spatial resolution, must be taken into account in analyzing and interpreting OMI data, particularly when creating maps from weighted data averages (see section 6).

[9] OMI's spatial resolution exceeds GOME's 320 × 40 km^2 resolution by a factor between 5 and 40 and SCIAMACHY's by a factor up to 5.7. Its daily global coverage is an improvement over that of GOME and SCIAMACHY, which provide the same coverage at intervals of 3 and 6 days, respectively. The daily global coverage is essential for applications such as estimating an atmospheric correction for ocean observing satellites (e.g., SeaWiFS).

[10] NO_2 vertical columns are computed from OMI data using the algorithm described by *Bucsela et al.* [2006]. We summarize the retrieval in sections 3, 4, and 5.

3. DOAS Retrieval

[11] The first step in the retrieval of NO_2 is the analysis of OMI spectra. The method used is Differential Optical Absorption Spectroscopy (DOAS) [*Platt and Stutz*, 2006], a spectral fitting technique that we apply in a window from 405 nm to 465 nm. In the current version, only two trace gas absorption spectra, namely NO_2 [*Vandaele et al.*, 1998] and O_3 [*Burrows et al.*, 1999a], are fitted to the measured spectra. Because of the wide fitting window, it is not necessary to include the relatively narrow absorptions from additional trace gases like O_2-O_2 and H_2O. Sensitivity studies using model spectra containing varying amounts of NO_2, the additional trace-gas absorption spectra and noise showed that fitting O_2-O_2 and H_2O did not affect the NO_2 retrieval. The fit is accomplished by minimizing the difference between measured and modeled radiances, i.e.,

$$\left[R(\lambda) - P_3(\lambda)(1 + \sigma_R(\lambda)C_R)e^{(-\sigma_{NO2}(\lambda)SCD_{NO2} - \sigma_{O3}(\lambda)SCD_{O3})}\right]^2 \rightarrow \min \quad (1)$$

with

$R(\lambda)$	ratio of Earthshine to incident solar spectra;
$\sigma(\lambda)$	absorption cross section for NO_2 and O_3;
SCD	slant column densities of NO_2 and O_3;
$P_3(\lambda)$	cubic polynomial to represent slowly varying functions;
$\sigma_R(\lambda)$	Raman radiance spectrum [*Chance and Spurr*, 1997];
C_R	Raman spectrum fit coefficient.

The result of the spectral fit is a slant column density (SCD) for each OMI pixel.

4. Air Mass Factor Correction

[12] The next step is the conversion of the slant column densities into vertical column densities. This is accomplished using the air mass factor (AMF) concept [*Solomon et al.*, 1987]:

$$VCD = \frac{SCD}{AMF} \tag{2}$$

[13] The AMF depends on a *differential AMF* profile, dAMF, a normalized a priori NO_2 profile n/VCD, and a temperature correction factor α. The AMF is calculated as follows:

$$AMF = \int_0^\infty dAMF(z) \cdot \alpha(z) \cdot \frac{n(z)}{VCD} \mathrm{dz}, \tag{3}$$

with

dAMF *differential AMF*, independent of NO_2 profile;
α correction factor, dependent on temperature profile;
n a priori NO_2 number density profile;
VCD NO_2 vertical column density of the a priori profile;
z altitude.

[14] The differential AMFs are independent of the NO_2 profile, but depend on viewing geometry, surface albedo, clouds and aerosols. Differential a priori AMFs are calculated for a range of conditions using the Radiative Transport Model TOMRAD [*Davé*, 1965] and stored in a look up table that is dependent on the five quantities: (1) solar zenith angle, (2) viewing zenith angle measured relative to the Earth's normal, (3) relative azimuth angle measured with respect to the Sun's location, (4) ground albedo, and (5) surface pressure. Because TOMRAD does not include partial or thin clouds, the radiative transfer calculations are carried out only for clear and overcast cases. In the latter, clouds are treated as opaque Lambertian surfaces with an albedo of 80%. AMFs for partly cloudy scenes are radiance weighted interpolations from clear sky AMFs and overcast AMFs, which are look up table entries with ground albedo set to the cloud albedo (80%) and surface pressure set to cloud top pressure as calculated by *Acarreta et al.* [2004]. The monthly climatology used for the ground albedo (including mean snow and ice cover) is from *Koelemeijer et al.* [2003] and cloud parameters are from *Acarreta et al.* [2004]. The effects of aerosols are not taken into account in the current version of the algorithm. For situations involving urban pollution, these effects are expected to be small ($\sim$5%) [*Martin et al.*, 2003].

[15] The temperature variation of the NO_2 absorption cross section [*Vandaele et al.*, 1998] is accounted for using a temperature-dependent correction factor $\alpha(z)$, which varies with altitude because of the altitude dependence of temperature. Although by formal definition, the air mass factor is independent of temperature, it is convenient to include the factor $\alpha(z)$ in the AMF calculation, as in equation (3). The factor is a function of the local atmospheric temperature profile and the fixed temperature of 220 K [*Vandaele et al.*, 1998] assumed in the DOAS fit. The operational algorithm employs monthly mean temperature profiles from NCEP [*Nagatani et al.*, 1990].

5. Estimation of Stratospheric and Tropospheric NO_2

[16] The stratospheric and tropospheric NO_2 columns are derived from the SCDs. In the case of OMI, the SCD field shows an instrumental artifact that must first be removed. The artifact is believed to result from CCD pixel damage due to transient events like radiation hits, which can cause long-term changes in pixel sensitivity or dark count [*Joiner and Vasilkov*, 2006]. The effect depends on the location of the pixel across the orbital track and varies slowly with time. Thus it leads to the appearance of "stripes" along the orbit when the data are mapped. The current operational algorithm corrects for this effect by adjusting the mean SCD for a given cross-track position to the mean value at all positions [*Celarier et al.*, 2008]. The mean SCD and the mean initial AMF for each cross-track position from 24 h of data using measurements obtained at latitudes between ±55° are computed and used to generate a set of 60 correction constants, one for each cross-track position, which are subtracted from the SCD values. At cross-track position i, the correction constant δ_i is computed as follows:

$$\delta_i = \langle \mathrm{SCD} \rangle_i - \langle \mathrm{AMF_S} \rangle_i \{ \langle \mathrm{SCD} \rangle_i \} / \{ \langle \mathrm{AMF_S} \rangle_i \}, \tag{4}$$

with $\langle\rangle$ standing for averaging along the orbit for the cross-track position i, and $\{\}$ for averaging over all cross-track positions.

[17] Using the NO_2 slant columns, the algorithm determines the stratospheric and tropospheric amounts of NO_2. To do this, the destriped SCDs are first converted to "initial VCDs" using an AMF calculated from the stratospheric profile (see Figure 2a) [*Douglass et al.*, 2003]. The resultant field is used to identify polluted regions, on the basis of the assumption that tropospheric NO_2 varies on much smaller spatial scales than stratospheric NO_2. Pollution source regions are masked a priori, and the remaining smooth stratospheric field is interpolated using a zonal planetary wave analysis that typically includes terms up to wave-2. The smooth field is subtracted from the initial field, and locations where the difference exceeds a predetermined threshold are assumed to be polluted. For these regions, a correction is applied using an AMF computed from a polluted profile:

$$\mathrm{VCD_T} = (\mathrm{SCD} - \mathrm{AMF_S VCD_S}) / \mathrm{AMF_T}, \tag{5}$$

where subscript S refers to the stratosphere and T refers to the troposphere.

[18] The dependence of the tropospheric AMF on the shape of the NO_2 profile varies with pollution amount. Thus, it is important to identify the locations of polluted

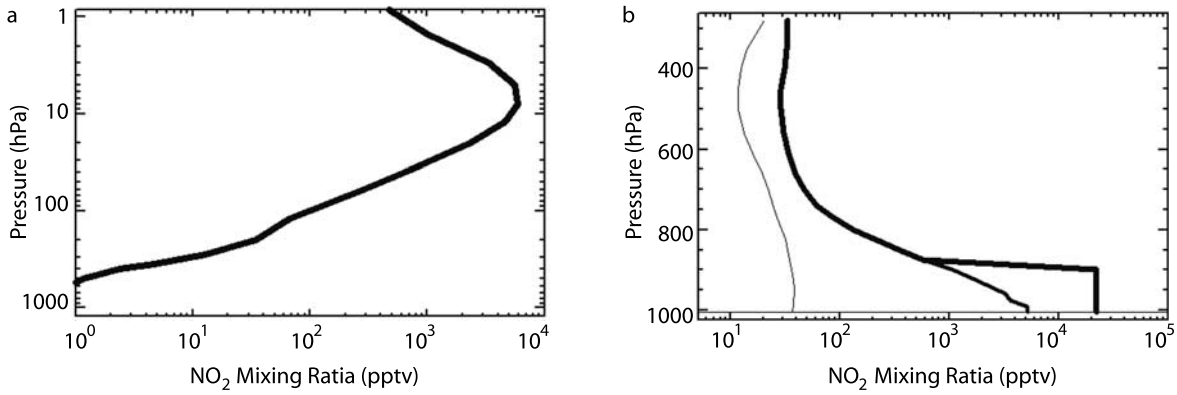

Figure 2. NO_2 concentration profiles used in the calculation of the air mass factors (AMFs). Shown are (a) the stratospheric profile n_S calculated using the GMI CTM [*Douglass et al.*, 2003] and (b) three examples of tropospheric profiles n_T for an ocean pixel (thin line), the GSFC pixel where the ground instrument is located (thick line), and the same profile with artificially increased boundary level pollution (thicker line). The polluted profiles are annual mean profiles computed by the Harvard GEOS-Chem model [*Bey et al.*, 2001].

pixels so that an appropriate NO_2 profile is used in the calculations. In the OMI algorithm, polluted profiles (see Figure 2b) are chosen from a look-up table of a geographically gridded (2.5° × 2.0°) set of annual mean profiles computed by the Harvard GEOS-Chem model [*Bey et al.*, 2001].

6. Gridded OMI NO_2 Data

[19] To visualize and compare the OMI NO_2 data with other data sets, the NO_2 VCDs are subset onto a longitude-

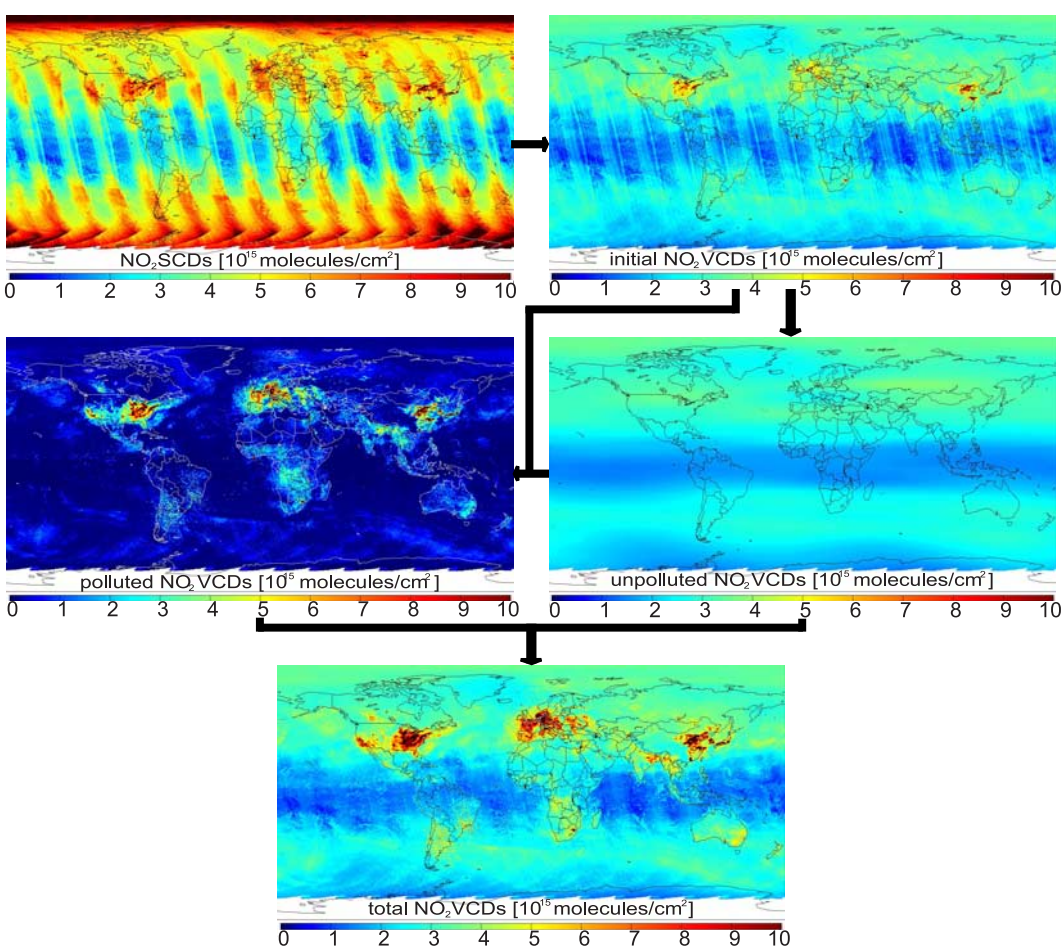

Figure 3. Flowchart of the OMI NO_2 vertical column retrieval algorithm.

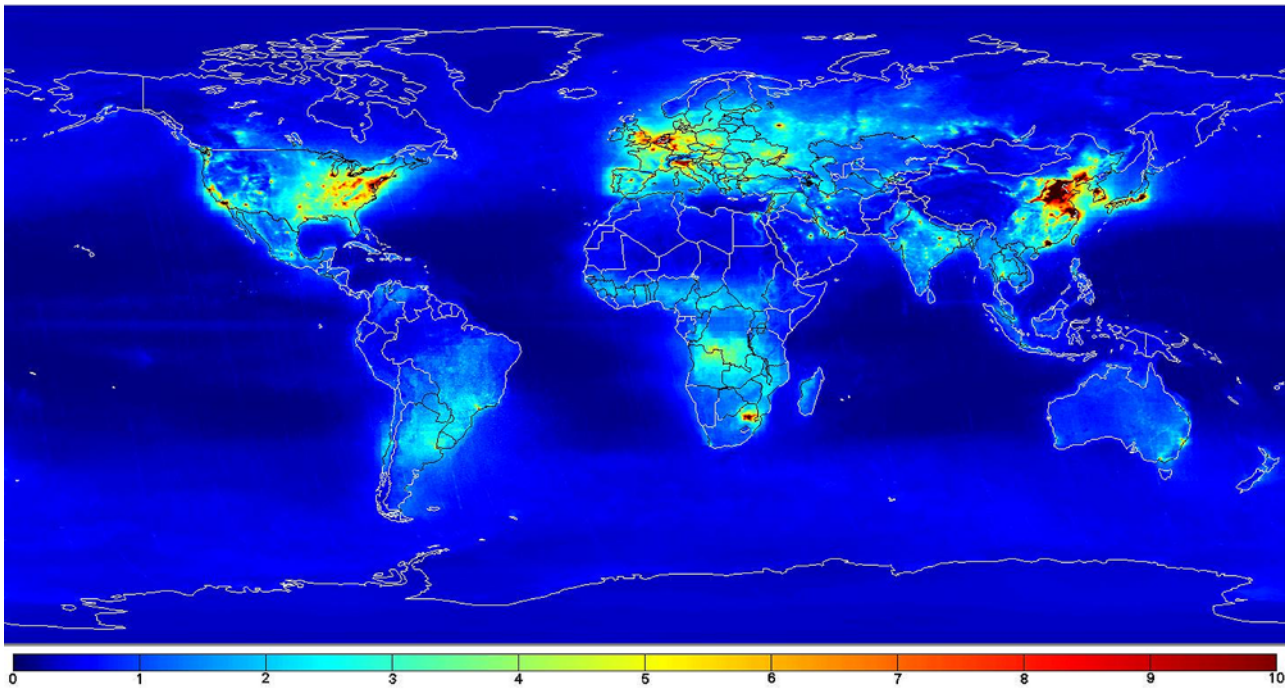

Figure 4. OMI tropospheric NO_2 vertical column densities, 2005 average (10^{15} molecules/cm^2), binned on a 0.25 × 0.25 deg^2 grid using the technique described in section 5.

latitude grid. The grid resolution used in this study is 0.02° and the cells are small compared to the size of a typical OMI pixel, e.g., 2.2 × 1.7 km^2 at 39° latitude. The gridded product is based on all VCDs observed within the specified period (e.g., 1 day, as in Figure 3, or 1 year, as in Figures 4 and 5) that have solar zenith angles less than 85° and were measured during the ascending phase of the orbit. For each OMI pixel the measured VCD is stored in all grid cells lying

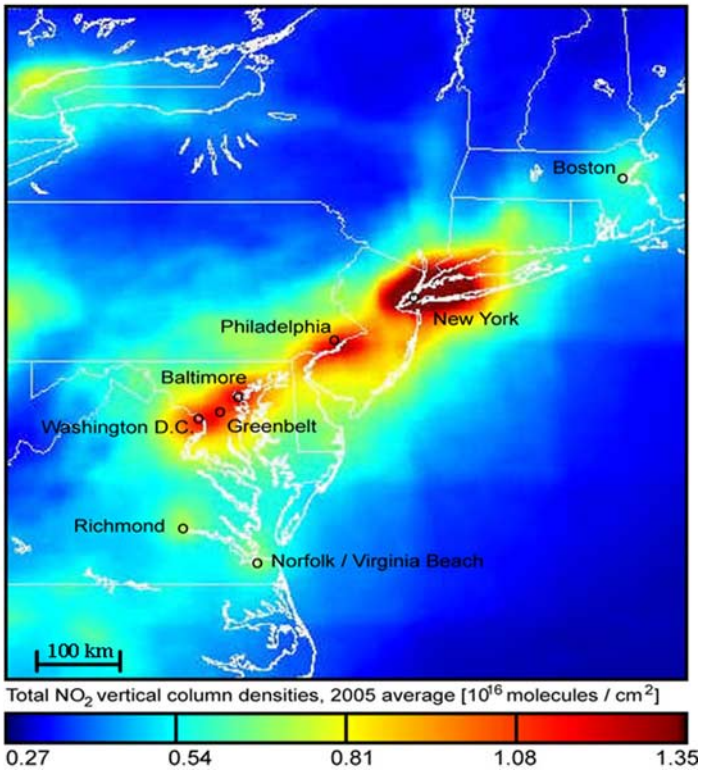

Figure 5. Total NO_2 vertical column densities, 2005 average, binned on a 0.02 × 0.02 deg^2 grid using the technique described in section 5.

within the pixel boundary. Where multiple pixels overlap, the VCD value for the grid cell is the weighted average of the OMI measurements.

[20] The weighting factor w for a grid cell can be thought of as the inverse of the squared error for the grid cell. If the absolute errors, σ_{VCDT}, in the tropospheric NO_2 vertical columns were independent of the values themselves, the optimal weights would be $1/\sigma^2_{\mathrm{VCDT}}$, which minimize the error in the average. However, the errors scale with the NO_2 VCD values due to the AMF dependence (see section 7.1), and weighting with $1/\sigma^2_{\mathrm{VCDT}}$ yields an average biased toward low VCD values. To avoid this bias we adopt the following grid cell weights for which only the dependence of the errors on the cloud cover, which was estimated to be 1.5×10^{15} (1 + 3C) (see section 7.1) multiplied with the area weight A, is used instead:

$$w = \frac{1}{A(1.5 \cdot 10^{15}\ (1 + 3 \cdot C))^2}, \tag{6}$$

where A is the area of the OMI pixel and C is the fractional cloud cover. For a single OMI pixel covering N grid cells, the dependence on area, A, in equation (6) ensures that individual grid cell errors are consistent with the error for the whole pixel; that is, the standard error in the mean (proportional to $N^{-1/2}$ or $A^{-1/2}$) of grid cells under an OMI pixel equals the OMI pixel error. With this weighting scheme, smaller OMI pixels are given more weight, which enhances the detail in the gridded NO_2 field. The averaging technique adopted in this study is most effective when averaging many overlapping pixels over long periods, (e.g., a year, see Figure 4). However, it is also useful for daily maps, which contain overlap between adjacent orbits as well as overlap within a single orbit caused by the "bow tie" shape of OMI scan lines (see Figure 1a).

7. Ground-Based Validation Measurements

[21] To validate the OMI NO_2 data, a comparison with ground-based measurements from a Brewer MK3 spectrometer was performed. The Brewer MK3 spectrometer is a double monochromator that measures the wavelength region between 283 nm and 364 nm. A more detailed description of the instrument has been published by *Cede et al.* [2006]. The instrument takes multiple measurements while viewing the direct Sun for 4 min per measurement set. Data sets are taken every ~30 min for SZA smaller than 80°. The spectral sampling ranges from 0.1 nm to 3 nm and the spectral resolution is 0.5 nm. The 0.1 nm sampled data was only taken around local noon, approximately 1.5 h before OMI overpass. For the NO_2 DOAS retrieval used in this study 6 wavelengths 3 nm apart in the interval 348–363 nm were used. Only the NO_2 cross section is fitted to the measured spectrum after structures caused by O_3 and O_2-O_2 have been removed. The cross sections used for the retrieval are from *Vandaele et al.* [1998] for NO_2 at 270 K, from *Burrows et al.* [1999a] for O_3, and from *Greenblatt et al.* [1990] for O_2-O_2. The instrument is located at the NASA Goddard Space Flight Center (38.98°N, 76.83°W, 90 m a.s.l.) in the Baltimore-Washington corridor, a region of more than 5 million people that experiences heavy automobile traffic and has major hydrocarbon based power generating plants.

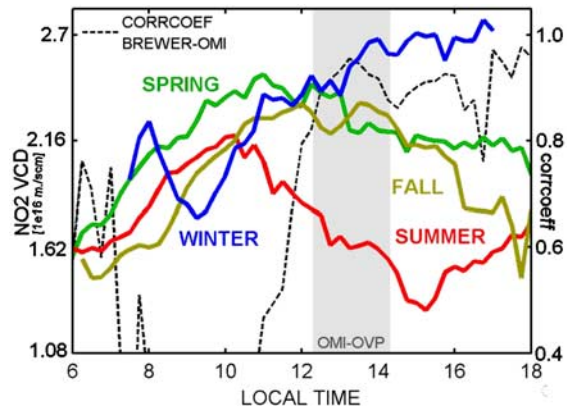

Figure 6. Average diurnal behavior of Brewer NO_2 total column at GSFC for meteorological seasons. Dashed black line shows the correlation coefficient between the OMI data and the Brewer data at different times of the day. Gray area indicates the OMI overpass time.

[22] For the comparison with OMI, only clear-sky data (effective cloud fraction less than 30%) were used, since clouds complicate the interpretation of ground based and satellite measurements. The stratospheric fraction of NO_2 has been estimated to be 0.1 DU and is subtracted from the measurement data to derive tropospheric values. This value had been derived from a cloud free day with minimal NO_2. Brewer data from 1215 to 1415 local time (which is the OMI overpass time and, therefore, shows the best correlation to OMI data, see Figure 6) were compared with OMI data averaged for all grid cells within either 15 km or 50 km of the ground station. To reduce the effect of natural and instrument noise variances, monthly means were used in the comparisons.

8. Uncertainty Analysis

[23] In this section we estimate the uncertainties in VCDs measured by the Brewer and the OMI instrument. For each uncertainty contribution, we distinguish between random and systematic components. We assume the random components to be statistically distributed and uncorrelated over time, while the systematic components are persistent and affect all measurements in the same way during a given period. This distinction depends on the selected period and is easily determined for some sources of uncertainty. Instrumental noise, for example, is a pure random uncertainty even for very short periods, while a calibration error is a pure systematic uncertainty for any length of time. However, in other cases, separating the two types of uncertainty is more difficult, e.g., in determining the influence of the atmospheric temperature. Over timescales of less than a day differences between the actual temperature and the one used in the NO_2 algorithm can be considered a systematic error. However, over weeks or months, such differences may have both a systematic component due to bias in the climatological temperature profile and a random component resulting from hourly and daily fluctuations about the climatological mean. In this study we require monthly means to reduce the noise in the ground measurements. In the following the random error sources for the

OMI data and the ground measurement data are described and the comparison of the two data sets will show if the resulting error bars are sufficient to explain differences and will also provide insights about unknown systematic error sources.

8.1. Uncertainties in the OMI Measurements

[24] Using equation (5) the uncertainty of the OMI tropospheric VCD is computed as follows:

$$\sigma_{VCDT}^2 = \left(\frac{1}{AMF_T}\right)^2 \cdot \sigma_{SCD}^2 + \left(\frac{SCD - AMF_S \cdot VCD_S}{AMF_T^2}\right)^2 \cdot \sigma_{AMFT}^2 + \left(\frac{VCD_S}{AMF_T}\right)^2 \cdot \sigma_{AMFS}^2 + \left(\frac{AMF_S}{AMF_T}\right)^2 \cdot \sigma_{VCDS}^2, \quad (7)$$

where σ_{AMFT}, σ_{AMFS} and σ_{VCDS} are the uncertainties in $\mathrm{AMF_T}$, $\mathrm{AMF_S}$ and $\mathrm{VCD_S}$ respectively. The slant column errors σ_{SCD} are approximately 0.7×10^{15} molecules cm^{-2} as estimated by *Boersma et al.* [2007] and are assumed to be random. For the stratospheric component of the observed column a random uncertainty of 0.2×10^{15} molecules cm^{-2} is estimated by applying the separation algorithm to CTM model data [*Bucsela et al.*, 2006].

[25] The algorithm uses two types of AMFs, the stratospheric AMF and the tropospheric AMF. The tropospheric AMF is a combination of $\mathrm{AMF_T^{clear}}$ and $\mathrm{AMF_T^{cloud}}$. For the stratospheric air mass factor $\mathrm{AMF_S}$, we do not distinguish between the clear- and cloudy-sky AMF because the difference is negligible. Each AMF varies with solar zenith angle (SZA), viewing zenith angle and relative azimuth angle (all via the dAMFs). Uncertainties in these angles are negligible, and the relative AMF uncertainties were found to be approximately independent of the viewing geometry. All three AMFs depend on the a priori profile shape (n_T and n_S, see Figure 2), although this dependence is negligible in the case of $\mathrm{AMF_S}$. $\mathrm{AMF_T^{cloud}}$ also depends on the cloud pressure $\mathrm{P_C}$, while $\mathrm{AMF_T^{clear}}$ depends on the terrain albedo $\mathrm{R_t}$ (both via the dAMFs). The cloud albedo $\mathrm{R_C}$ is fixed at 0.8 [*Acarreta et al.*, 2004].

[26] Clear- and cloudy-sky AMF uncertainties are estimated using simple empirical expressions derived from an analysis of one month of GEOS-Chem and GSFC CTM model output. This analysis included about 800 midnorthern latitude daily NO_2 profiles for low, moderate and highly polluted conditions. AMFs were computed for each profile and a variety of values of $\mathrm{R_t}$. The relative uncertainties reflect profile shape variation and the uncertaintie σ_{Rt}. Based in this data we derived an empirical function for the tropospheric clear-sky AMF:

$$\sigma_{\mathrm{AMFT}}^{\mathrm{clear}} = \mathrm{AMF_T^{clear}} / \left[300 \cdot (\mathrm{R_t} - 2 \cdot \sigma_{\mathrm{Rt}} + 0.12)^2\right] \quad (8)$$

This fitted function matches the data well, except for very low terrain albedos with large uncertainties. Note that when the terrain albedo is about 0.05 and its uncertainty is small, the profile variation alone leads to an AMF uncertainty of about 15%. This is consistent with the findings of *Boersma et al.* [2004]. A terrain albedo uncertainty of $\sigma_{\mathrm{Rt}} = 0.015$ is used in the OMI NO_2 algorithm, which is approximately the value given by *Koelemeijer et al.* [2003] for wavelengths used in NO_2 retrievals. To a first-order approximation, the cloudy-sky tropospheric AMF was found to follow the empirical expression

$$\sigma_{\mathrm{AMFT}}^{\mathrm{cloud}} = \mathrm{AMF_T^{cloud}} 0.8\rho \quad (9)$$

where ρ is the fraction of the a priori polluted NO_2 column below cloud level. This expression is valid when the cloud pressure and its uncertainty are relatively low.

[27] The total tropospheric air mass factor, $\mathrm{AMF_T}$, and its uncertainty, σ_{AMFT}, are computed from the clear and cloudy components. The expression for the tropospheric AMF is

$$\mathrm{AMF_T} = w\mathrm{AMF_T^{cloud}} + (1 - w)\mathrm{AMF_T^{clear}} \quad (10)$$

For a polluted region like the Washington DC area, typical values for $\mathrm{AMF_T^{cloud}}$ are less than 0.1, while typical values for $\mathrm{AMF_T^{clear}}$ are about 0.7. The cloud radiance fraction, w, is related to the effective geometrical cloud fraction f [*Acarreta et al.*, 2004] by:

$$w = \frac{f\, I_{cloud}}{f\, I_{cloud} + (1 - f) I_{clear}} \quad (11)$$

Here I_{clear} and I_{cloud} are the radiances of clear and cloudy scenes, respectively. The uncertainty σ_w is approximately given by:

$$\sigma_w \approx \sigma_f (w(1 - w))/(f(1 - f)) \quad (12)$$

We assume an uncertainty in the cloud fraction $\sigma_f = 0.02$, which is the estimate from *Boersma et al.* [2004]. The uncertainty for the tropospheric AMF is

$$\sigma_{AMFT}^2 = \left(\mathrm{AMF_T^{cloud}} - \mathrm{AMF_T^{clear}}\right)^2 \sigma_w^2 + w^2 \left(\sigma_{\mathrm{AMFT}}^{\mathrm{cloud}}\right)^2 + (1 - w)^2 \left(\sigma_{\mathrm{AMFT}}^{\mathrm{clear}}\right)^2 \quad (13)$$

AMF uncertainties range from approximately 20% for low cloud fraction to 50–80% for high cloud fraction, depending on profile shape and cloud top height.

[28] Stratospheric air mass factors, $\mathrm{AMF_s}$, depend mainly on viewing geometry and are essentially independent of cloud cover, albedo or profile shape. Model analysis showed that the combination of these effects introduces an uncertainty of 1–2% in the AMF. A conservative relative uncertainty of 2% was assigned to all stratospheric air mass factors.

$$\sigma_{\mathrm{AMFS}} = 0.02\, \mathrm{AMF_S} \quad (14)$$

The AMF uncertainties introduce errors in the OMI tropospheric column, which are a combination of random and systematic errors. For the generation of monthly mean values used in this study, the uncertainties were propagated as random errors (error bars in Figure 7). Only days where both instruments could measure were used for this averaging process. The derived uncertainties for most daily clear sky values of tropospheric NO_2 range from 40 to 80%.

8.2. Uncertainties in the Ground Measurements

[29] The uncertainty estimations for $\mathrm{VCD_{BREW}}$ are based on a study performed by *Cede et al.* [2006]. Equation (2)

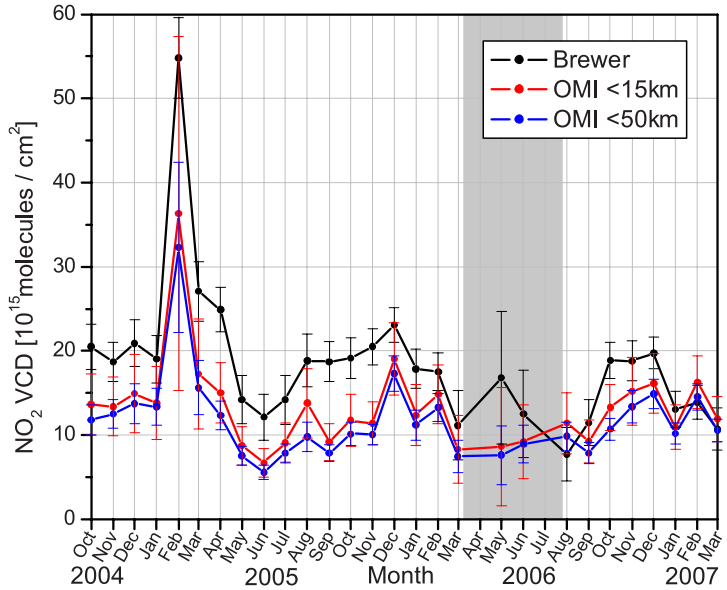

Figure 7. Monthly mean NO_2 tropospheric columns. Brewer data are cloud-screened temporal averages around OMI overpass time. The gray rectangle indicates a period when the Brewer data are very sparse. Satellite data are spatial averages over pixels centered within 15 km (red) or 50 km (blue) of the ground location.

shows that the uncertainty in VCD_{BREW} ($\sigma_{VCDBREW}$) is a combination of the uncertainties in SCD_{BREW} ($\sigma_{SCDBREW}$) and AMF_{DIRSUN}. For SZA < 80°, the uncertainty in AMF_{DIRSUN} is less than 1% and, therefore negligible compared to $\sigma_{SCDBREW}$. Therefore we can express the uncertainty of the Brewer measurement by:

$$\sigma_{VCDBREW} = \frac{1}{AMF_{DIRSUN}} \sigma_{SCDBREW} \tag{15}$$

In equation (15), $\sigma_{VCDBREW}$ includes instrumental noise (photon counting noise), possible instrumental drifts, atmospheric noise (atmospheric variations over the measurement duration of 4 min), aerosol effects, variation in other absorbing gases (O_3, HCHO, BrO), variations in temperature profile, surface pressure, the stratospheric NO_2 column. For cloud-screened data, these random components range from 0.15 to 0.40 DU (1 DU = 2.7 10^{16} molecules/cm^2) and are driven primarily by instrumental and atmospheric noise.

[30] Instrumental noise can be large, since the DOAS fit is based on only 6 wavelengths. However, because such noise is a pure random error, averaging can reduce its influence. In this study, a minimum of N = 2 cloud-screened measurements during the 2-h window (1220–1420 local time) around OMI overpass time were averaged. Typically there are N = 4 such measurements per day, which reduces instrumental noise by a factor of 2. For monthly means of the daily values (N > 60) the noise does not exceed 0.05 DU, and is negligible compared to the differences between the Brewer and OMI values shown in Figure 7.

[31] The sources of the systematic component include calibration, instrumental drifts, nonlinear aerosol effects, influence of other absorbing gases (O_3, HCHO, and BrO), and temperature profile and surface pressure. The uncertainty due to two of these contributions, calibration and instrumental drift, does not depend on AMF_{DIRSUN} and is estimated to be σ_{SCDB_SYS1} = 0.22 DU. The uncertainty for all other systematic effects increases with AMF_{DIRSUN}. This component is estimated to 0.13 DU.

[32] We combine the individual uncertainty estimates to obtain total expanded uncertainties for monthly mean ground measurements of NO_2 near OMI overpass time at GSFC. The result is $\sigma_{VCDBREW}$ = 0.17 DU in December (mean AMF_{DIRSUN} = 2.67) and $\sigma_{VCDBREW}$ = 0.26 DU in June (mean AMF_{DIRSUN} = 1.14). Because of the nature of the direct-Sun measurements, the Brewer uncertainties are absolute numbers. In contrast, uncertainties in OMI NO_2 are better expressed as a fraction of the measured NO_2 VCDs. This follows from the fact that OMI vertical column errors are dominated by errors in the AMF, which scales the slant column measurements.

9. Results

[33] As seen in Figure 7, both the ground data and the satellite data show a pronounced seasonal cycle, with generally higher NO_2 values in winter and lower values in summer. The monthly mean ground measurements and the satellite data are approximately proportional, but the proportionality for the last year is distinctly different from that for the first 2 years. The Pearson correlation coefficients between the two data sets are 0.88 for OMI data within 50 km of the ground measurement site and 0.90 for data within 15 km. OMI data within 15 km are 25% lower than the Brewer data, on average. A total least squares regression was performed on the monthly mean values with the data weighted by the 2σ uncertainties for both instruments as described in section 7. The result was a slope of 0.75(±0.14) and a y intercept of −0.38(±2.5) × 10^{15} molecules/cm^2. The correlation coefficient for the daily values is 0.58. A line fitted to these data and forced through the origin has a very similar slope of 0.76 ± 0.009.

[34] The error bars are large for months in which only a small number of coinciding measurements were available, e.g., March, May and June 2006. However, for most other months, the 2σ error bars for the OMI and Brewer data do not overlap. This comparison shows that the difference is larger than the error bars based on random errors would indicate. The uncertainties in the OMI data may be greater than the derived error bars indicate, since unknown systematic errors in the a priori profiles and ground albedos may not be fully accounted for in the OMI uncertainty estimates and therefore not reduced by averaging.

[35] We examined a number of possible reasons for the differences between the OMI and Brewer data. To determine whether aerosol contamination may account for some of the discrepancy, we compared the difference between the two data sets to the 440 nm aerosol optical thickness (AOT) data set from the GSFC site of the Aerosol Robotic Network (Aeronet) [*Holben et al.*, 2001]. Results indicated no obvious correlation between the NO_2 and aerosol data. Aerosol AOT determined by AERONET agrees with the direct-Sun AOT measurements made by the Brewer. We estimate that 5–10% of the difference may be explained by the difficulty in averaging OMI data near a "hot spot," where the spatial gradients in NO_2 amounts are high (see Figure 5). Figure 7 shows that larger OMI NO_2 columns are obtained when a smaller radius is used for averaging (15 km instead of 50 km).

[36] The remaining 15–20% of the discrepancy may result from errors in the OMI AMF. This error is mainly due to a combination of incorrect assumptions regarding ground albedo and the NO_2 profile shape used for the AMF calculation. Underestimating the proportion of NO_2 in the boundary layer yields an overestimation of the AMF and a resultant underestimation of the OMI NO_2 vertical column amount. To quantify the sensitivity of the OMI retrievals to profile shape, we increased the mixing ratios in the boundary layer for the a priori profile used in the AMF calculation (Figure 2b). The boundary layer height is assumed to be 1 km and the surface mixing ratio is set to 22 ppb. This mixing ratio is based on air quality trends as reported at http://nsdi.epa.gov/air/airtrends/nitrogen.html. The AMFs computed from this artificial profile would increase the OMI NO_2 amounts by 3–7% depending on the ground albedo. Increasing the boundary layer height to 1.5 km would decrease the NO2 VCDs by ~3% and decreasing the boundary layer height to 0.5 km would increase the values by 7–15%.

[37] A comparison of the 380 nm ground albedo as estimated by [*Koelemejer et al.*, 2003] using the same algorithm as the one used to calculate the 440 nm albedo data set, and the 380 nm ground albedo as estimated by [*Herman and Celarier*, 1997] suggest an overestimation of the ground albedo used in this study by several percentage points. Such an overestimation would lead to a systematic underestimation of the derived NO_2 VCDs of up to 25%, which is the same size as the observed differences between OMI and the Brewer VCDs. It is also possible that spatial gradients within the 15 km radius between the OMI pixels and the Brewer spectrometer location could account for some of the discrepancy. These two errors are systematic, and accounting for either of them would increase the OMI NO_2 amounts and thereby reduce the discrepancy with the Brewer data. The profile shape assumption error could increase or decrease OMI NO_2 and may vary from day-to-day or with season. The differences between the OMI and the Brewer data do not show a seasonal dependence, so error sources with a seasonal dependence (e.g., profile shape, snow cover, etc.) are unlikely to explain the discrepancy.

10. Summary and Conclusions

[38] In this paper, we have described the algorithm used to retrieve tropospheric NO_2 vertical column densities from OMI and discussed validation of the retrieval using ground-based data at one location. The OMI algorithm uses the DOAS technique to determine NO_2 slant column densities and applies stratospheric AMFs to compute an initial VCD field. Filtering and interpolation techniques are used to identify polluted regions, and polluted VCDs are computed using appropriate tropospheric AMFs.

[39] OMI measurements were compared to ground-based data in a validation study using the Brewer MK3 spectrometer located at NASA Goddard Space Flight Center, Greenbelt, MD, USA. A time series using monthly averaged Brewer NO_2 columns appear consistently 25% higher than the OMI data retrieved within 15 km of the Brewer. However, the correlation between the Brewer and the OMI time series is good (r = 0.9). The relative differences between the two data sets may be attributable to errors in the assumed ground albedo and/or the a priori NO_2 profile shapes assumed in the OMI retrieval algorithm. Such errors can systematically affect the tropospheric NO_2 columns obtained from OMI. An additional factor may be spatial gradients in the NO_2 field around the measurement site at GSFC. Large gradients can lead to varying differences between the averages of OMI pixel values and the ground measurements, depending on the area over which the averages are taken. Other discussed errors are small by comparison.

References

Acarreta, J. R., J. F. deHaan, and P. Stammes (2004), Cloud pressure retrieval using the O_2-O_2 absorption band at 477 nm, *J. Geophys. Res.*, *109*, D05204, doi:10.1029/2003JD003915.

Beirle, S., et al. (2005), Estimating the NO_x produced by lightning from GOME and NLDN data: A case study in the Gulf of Mexico, *Atmos. Chem. Phys. Discuss.*, *5*, 11,295–11,329.

Bey, I., D. J. Jacob, R. M. Yantosca, J. A. Logan, B. D. Field, A. M. Fiore, Q. Li, H. Y. Liu, L. J. Mickley, and M. G. Schultz (2001), Global modeling of tropospheric chemistry with assimilated meteorology: Model description and evaluation, *J. Geophys. Res.*, *106*, 23,073–23,096, doi:10.1029/2001JD000807.

Boersma, K. F., H. J. Eskes, and E. J. Brinksma (2004), Error analysis for tropospheric NO_2 retrieval from space, *J. Geophys. Res.*, *109*, D04311, doi:10.1029/2003JD003962.

Boersma, K. F., et al. (2007), Near-real time retrieval of tropospheric NO_2 from OMI, *Atmos. Chem. Phys.*, *7*, 2103–2118.

Bovensmann, H., J. P. Burrows, M. Buchwitz, J. Frerick, V. V. Rozanov, K. V. Chance, and A. P. H. Goede (1999), SCIAMACHY: Mission objectives and measurement modes, *J. Atmos. Sci.*, *56*, 127–150, doi:10.1175/1520-0469(1999)056<0127:SMOAMM>2.0.CO;2.

Brewer, A. W., C. T. McElroy, and J. B. Kerr (1973), Nitrogen dioxide concentrations in the atmosphere, *Nature*, *246*(5429), 129–133, doi:10.1038/246129a0.

Bucsela, E. J., E. A. Celarier, M. O. Wenig, J. F. Gleason, J. P. Veefkind, K. F. Boersma, and E. Brinksma (2006), Algorithm for NO_2 vertical column retrieval from the Ozone Monitoring Instrument, *IEEE Trans. Geosci. Remote Sens.*, *44*(5), 1245–1258, doi:10.1109/TGRS.2005.863715.

Burrows, J. P., A. Richter, A. Dehn, B. Deters, S. Himmelmann, S. Voigt, and J. Orphal (1999a), Atmospheric remote sensing reference data from GOME: 2. Temperature-dependent absorption cross-sections of O3 in the 231–794 nm range, *J. Quant. Spectrosc. Radiat. Transfer*, *61*, 509–517, doi:10.1016/S0022-4073(98)00037-5.

Burrows, J., et al. (1999b), The Global Ozone Monitoring Experiment (GOME): Mission concept and first scientific results, *J. Atmos. Sci.*, *56*, 151–175, doi:10.1175/1520-0469(1999)056<0151:TGOMEG>2.0.CO;2.

Cede, A., J. Herman, A. Richter, N. Krotkov, and J. Burrows (2006), Measurements of nitrogen dioxide total column amounts using a Brewer double spectrometer in direct Sun mode, *J. Geophys. Res.*, *111*, D05304, doi:10.1029/2005JD006585.

Celarier, E. A., et al. (2008), Validation of Ozone Monitoring Instrument nitrogen dioxide columns, *J. Geophys. Res.*, *113*, D15S15, doi:10.1029/2007JD008908.

Chance, K., and R. J. D. Spurr (1997), Ring effect studies: Rayleigh scattering, including molecular parameters for rotational Raman scattering, and the Fraunhofer spectrum, *Appl. Opt.*, *36*, 5224–5230.

Crutzen, P. J. (1970), The influence of nitrogen oxides on the atmospheric ozone content, *Q.J.R. Meteorol. Soc.*, *96*, 320–325, doi:10.1002/qj.49709640815.

Crutzen, P., and U. Schmailzl (1983), Chemical budgets of the stratosphere, *Planet. Space Sci.*, *31*, 1009–1020, doi:10.1016/0032-0633(83)90092-2.

Davé, J. V. (1965), Multiple scattering in a non-homogeneous Rayleigh atmosphere, *J. Atmos. Sci.*, *22*, 273–279, doi:10.1175/1520-0469(1965)022<0273:MSIANH>2.0.CO;2.

Douglass, A. R., M. R. Schoeberl, R. B. Rood, and S. Pawson (2003), Evaluation of transport in the lower tropical stratosphere in a global chemistry and transport model, *J. Geophys. Res.*, *108*(D9), 4259, doi:10.1029/2002JD002696.

Granli, T., and O. Bokman (1994), Nitrous oxides from agriculture, *Norw. J. Agric. Sci.*, *12*, 1–128.

Greenblatt, G. D., J. J. Orlando, J. B. Burkholder, and A. R. Ravishankara (1990), Absorption measurements of oxygen between 330 and 1140 nm, *J. Geophys. Res.*, *95*(D11), 18,577–18,582, doi:10.1029/JD095iD11p18577.

Heland, J., H. Schlager, A. Richter, and J. P. Burrows (2002), First comparison of tropospheric NO_2 column densities retrieved from GOME measurements and in situ aircraft profile measurements, *Geophys. Res. Lett.*, *29*(20), 1983, doi:10.1029/2002GL015528.

Herman, J. R., and E. Celarier (1997), Earth surface reflectivity climatology at 340 nm to 380 nm from TOMS data, *J. Geophys. Res.*, *102*, 28,003–28,011, doi:10.1029/97JD02074.

Holben, B. N., et al. (2001), An emerging ground-based aerosol climatology: Aerosol optical depth from AERONET, *J. Geophys. Res.*, *106*, 12,067–12,097.

Joiner, J., and A. P. Vasilkov (2006), First results from the OMI rotational Raman scattering cloud pressure algorithm, *IEEE Trans. Geosci. Remote Sens.*, *44*(5), 1272–1282, doi:10.1109/TGRS.2005.861385.

Koelemeijer, R. B. A., J. F. De Haan, and P. Stammes (2003), A database of spectral surface reflectivity in the range 335–772 nm derived from 5.5 years of GOME observations, *J. Geophys. Res.*, *108*(D2), 4070, doi:10.1029/2002JD002429.

Lee, D. S., I. Köhler, E. Grobler, F. Rohrer, R. Sausen, L. Gallardo-Klenner, J. G. J. Olivier, F. J. Dentener, and A. F. Bouwman (1997), Estimations of global NOx emissions and their uncertainties, *Atmos. Environ.*, *31*, 1735–1749, doi:10.1016/S1352-2310(96)00327-5.

Martin, R. V., D. J. Jacob, K. Chance, T. P. Kurosu, P. I. Palmer, and M. J. Evans (2003), Global inventory of nitrogen oxide emissions constrained by space-based observations of NO2 columns, *J. Geophys. Res.*, *108*(D17), 4537, doi:10.1029/2003JD003453.

Martin, R. V., D. D. Parrish, T. B. Ryerson, D. K. Nicks Jr., K. Chance, T. P. Kurosu, D. J. Jacob, E. D. Sturges, A. Fried, and B. P. Wert (2004), Evaluation of GOME satellite measurements of tropospheric NO_2 and HCHO using regional data from aircraft campaigns in the southeastern United States, *J. Geophys. Res.*, *109*, D24307, doi:10.1029/2004JD004869.

Nagatani, R. M., A. J. Miller, K. W. Johnson, and M. E. Gelman (1990), An eight-year climatology of meteorological and SBUV ozone data, *NOAA Tech. Rep., 17*, 333 pp., NOAA, Camp Springs, Md.

Noxon, J. F. (1975), Nitrogen dioxide in the stratosphere and troposphere measured by ground-based absorption spectroscopy, *Science*, *189*, 547–549.

Noxon, J. F. (1979), Stratospheric NO_2: 2. Global behavior, *J. Geophys. Res.*, *84*(C8), 5067–5076.

Noxon, J. F., E. C. Whipple Jr., and R. S. Hyde (1979), Stratospheric NO_2: 1. Observational method and behavior at mid-latitude, *J. Geophys. Res.*, *84*(C8), 5047–5065.

Platt, U., and J. Stutz (2006), *Differential Optical Absorption Spectroscopy (DOAS), Principle and Applications*, Springer, Heidelberg, Germany.

Solomon, S., and R. R. Garcia (1984), On the distribution of long-lived tracers and chlorine species in the middle atmosphere, *J. Geophys. Res.*, *89*, 11,633–11,644.

Solomon, S., A. L. Schmeltekopf, and R. W. Sanders (1987), On the interpretation of zenith sky measurements, *J. Geophys. Res.*, *92*(D7), 8311–8319, doi:10.1029/JD092iD07p08311.

Solomon, S., R. W. Portmann, R. W. Sanders, J. S. Daniel, W. Madsen, B. Bartram, and E. G. Dutton (1999), On the role of nitrogen dioxide in the absorption of solar radiation, *J. Geophys. Res.*, *104*, 12,047–12,058, doi:10.1029/1999JD900035.

Vandaele, A. C., C. Hermans, P. C. Simon, M. Carleer, R. Colin, S. Fally, M. F. Mérienne, A. Jenouvrier, and B. Coquart (1998), Measurements of the NO_2 absorption cross-section from 42000 cm^{-1} to 10000 cm^{-1} (238–1000 nm) at 220 K and 294 K, *J. Quant. Spectrosc. Radiat. Transfer*, *59*, 171–184, doi:10.1016/S0022-4073(97)00168-4.

K. F. Boersma, Department of Atmospheric Chemistry, Harvard University, Cambridge, MA 02138, USA.

E. J. Brinksma and J. P. Veefkind, Royal Netherlands Meteorological Institute, NL-3730 AE De Bilt, Netherlands.

E. J. Bucsela, NASA GSFC, Goddard Earth Sciences and Technology Center, University of Maryland, Baltimore County, Baltimore, MD 21250, USA.

A. M. Cede, NASA GSFC, Earth System Science Interdisciplinary Center, University of Maryland, College Park, MD 20740, USA.

E. A. Celarier, NASA GSFC, SGT Inc., Greenbelt, MD 20770, USA.

J. F. Gleason and J. R. Herman, NASA Goddard Space Flight Center, Code 613.3, Greenbelt, MD 20771, USA.

M. O. Wenig, Department of Physics and Materials Science, City University of Hong Kong, Kowloon, Hong Kong. (mark.wenig@cityu.edu.hk)